Corrosion Science 211 (2023) 110901

Contents lists available at ScienceDirect

Corrosion Science

journal homepage: www.elsevier.com/locate/corsci

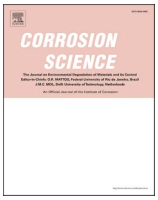

Pitting corrosion – Preferred chloride diffusion pathways in physical vapor deposited AlCrN coatings

O.E. Hudak [a,*], A. Bahr [a], P. Kutrowatz [a], T. Wojcik [a], F. Bohrn [a], L. Solyom [a], R. Schuster [b], L. Shang [c], O. Hunold [c], P. Polcik [d], M. Heller [e], P. Felfer [e], G. Ball [f], H. Riedl [a,g]

[a] Christian Doppler Laboratory for Surface Engineering of high-performance Components, TU Wien, Austria
[b] Christian Doppler Laboratory for Interfaces and Precipitation Engineering CDL-IPE, Institute of Materials Science and Technology, TU Wien, 1060, Vienna, Austria
[c] Oerlikon Balzers, Oerlikon Surface Solutions AG, 9496 Balzers, Liechtenstein
[d] Plansee Composite Materials GmbH, D-86983 Lechbruck am See, Germany
[e] Department of Materials Science, Friedrich-Alexander-Universität Erlangen-Nürnberg, Germany
[f] Institute of Chemical Technologies and Analytics, TU Wien, A-1060 Wien, Austria
[g] Institute of Materials Science and Technology, TU Wien, A-1060 Wien, Austria

ARTICLE INFO

Keywords:
PVD Coatings
Pitting Corrosion
Tafel-Plots
APT
TOF-SIMS
Chloride Diffusion

ABSTRACT

Pitting corrosion of sputtered and arc evaportaed fcc-AlCrN coated low-alloy steel substrates was studied in a 0.1 M NaCl solution, using a three-electrode-cell. Depending on the deposition technique, several diffusion mechanisms were identified by high-resolution techniques (i.e. APT, TOF-SIMS). For arc evaporated AlCrN, incoherently embedded macro-particles provided the majority of fast-track diffusion pathways and pit-initiation sites, while their pristine coating matrix proved protective against chloride inward diffusion. Contrarily, the more coarse-grained sputtered AlCrN morphology with a highly orientated crystal growth featured diffusion paths along column boundaries, where chloride permeated the coating structure and initiated pit formations at the coating-substrate interface.

1. Introduction

Corrosion processes epitomize the chemical interaction between a material and its surrounding, which ultimately leads to an altered or even degradative state of the material itself. Particularly saline environments represent a technological frontier, where machining elements suffer accelerated breakdown through a localized corrosion mechanism called – pitting. Being a highly insidious and self-sustaining process, pitting corrosion consistently shortens the lifespan of operating elements [1–3]. Therefore, the pitting behavior is an essential variable that, if properly understood, may drastically extend the longevity of material components.

The ingenuity of next-generation physical vapor deposited (PVD) coatings has given rise to a wide range of material concepts and has become a profitable method amongst high-tech industries. Particularly for technological avenues where there is no practicable low-priced bulk material at disposal, coatings provide a lucrative solution for protecting highly stressed machining components. For this reason, more and more industries resort to the application of protective coatings through means of sputtering and arc evaporation, rather than investing in the development of high-end bulk materials. However, with current state-of-the-art corrosion resistant coatings being far from optimized, it is of great interest to further investigate the fundamental mechanisms and underlying driving forces that dominate the degradative process.

Several corrosion mechanisms exist through which a coating can lose its protective quality: *(i)* local de-passivation by film-breakdown [4–6]; *(ii)* local delamination of the coating, caused by inward diffusion of corrosive media followed by the formation of corrosion products at the coating-substrate interface [7]; *(iii)* direct bypass of corrosive media at pin-holes [8,9]; and *(iv)* anodic dissolution of embedded metal based macroparticles [9–12], where the latter particularly pertains to cathodic arc evaporated (cae) thin films.

It is no secret that the production of metallic-macroparticles (droplets) during PVD processes poses a significant drawback in light of the coating's corrosion resistance [13]. Voids and rugged grain boundaries that surround such droplets, allow for fast-tracked diffusion of corrosive media to the substrate-coating interface. Furthermore, weakly bonded macroparticles may become dislodged from the coating matrix and

* Corresponding author.
E-mail address: oliver.hudak@tuwien.ac.at (O.E. Hudak).

https://doi.org/10.1016/j.corsci.2022.110901
Received 11 October 2022; Received in revised form 21 November 2022; Accepted 3 December 2022
Available online 6 December 2022

produce pin-holes that may function as initiation sites for localized corrosion.

For instance, Abusuilik and Inoue [10] have identified surface droplets and inclusions as particularly susceptible to corrosive attack, and illustrated how intermediate surface treatments can improve the corrosion resistance of arc evaporated CrN coating-substrate systems. Furthermore, Cedeño-Vente et al. [12] highlighted the relationship between macroparticle-size, deposition conditions, and corrosion behavior in aqueous NaCl-rich media for arc evaporated CrN coatings. However, not only arc-coatings with their evenly distributed droplets are vulnerable to corrosion, but also sputtered coatings have their weak spots. A study from Panjan et al. [9] on sputtered TiAlN hard coatings also identifies growth defects and pin-holes as significant contributors for pit-formations. Also combinations of arc evaporated and sputtered coating systems have been investigated, such as the CrN/NbN multilayer system by Wang et al. [11], with similar conclusions, namely, that macroparticles and growth defects stand at the center of the pitting mechanisms.

Despite these findings, transition metal nitrides (TMN) remain a versatile representative in the realm of protective coatings, convincing with good thermal stability, outstanding hardness, as well as noticeable oxidation and corrosion resistance [14–17].

This paper aims to expose possible diffusion pathways of chloride-rich media in both, arc evaporated- and sputtered AlCrN coatings beyond the already known diffusion routes along defect-sites and embedded macroparticles. We intend to first verify the aforementioned fast-track diffusion routes, upon which the focus will be extended to diffusion pathways through pristine, unimpaired coating sites that in theory should provide the best corrosion protection possible.

2. Experimental methods

2.1. Deposition parameters

All coatings were deposited in an industrial scale deposition system (INNOVA, Oerlikon Surface Solutions AG, Balzers). AlCr (70/30 at. %) targets were powder-metallurgically manufactured by Plansee Composite Materials GmbH and used for all, arc evaporated- and sputtered-coating variants. Single-crystalline Si-stripes (100-oriented, 20x7x 0.38 mm^3), 0.05 mm thick steel-foil, and low-alloy steel rounds (90MnCrV8) were utilized as substrates. Whereas coated Si-strips and steel-foil were solely used for as-deposited characterizations (e.g. analysis of the coatings morphology via fracture cross-section, coating thickness measurements and crystal-phase investigations by X-ray diffraction (XRD)), the coated low-alloy steel rounds were exclusively used for electrochemical-corrosion experiments and post-corrosion analysis. All substrates were ultrasonically cleaned with acetone and ethanol before mounting them into the deposition chamber. With a base pressure of at least $5{\cdot}10^{-3}$ Pa, the substrates were further cleaned for 25 min by a central-beam etching procedure (Oerlikon Surface Solutions AG).

All sputtered coatings were deposited at 500 °C, at a deposition pressure of 1.3 Pa, with a DC-bias voltage of −160 V and an Ar/N_2 ratio of 70/30, respectively. The arc evaporated coatings were grown at slightly lower temperature (480 °C), in a pure N_2 atmosphere at 3.2 Pa and a bias voltage of up to −100 V.

2.2. Structural and morphological characterization

For studying the morphology of the coatings, such as thickness, surface texture, and the integrity of the substrate-coating interfaces, a Zeiss Sigma 500 VP high-resolution field emission gun scanning electron microscope (FEGSEM) was used. With an acceleration voltage, ranging between 3 kV and 7 kV, characterization of coating thickness and coating morphology were performed on fracture cross sections of coated steel-foil substrates. Equipped with an EDAX Octane elect system, energy dispersive spectroscopy (EDS) was utilized for quantitative elemental investigations. Moreover, transmission electron back scattered diffraction (t-EBSD) was done to obtain an averaged evaluation of the as-deposited grain-size distribution of both, sputtered and arc evaportaed samples, as well as to gain knowledge about possible texturisation and preferred growth orientations (Velocity Super, EDAX).

For a more detailed investigation of the coating morphologies, transition electron microscopy (TEM, FEI TECNAI F20) was conducted. Bright field (BF) imaging was utilized to learn more about the microstructure, crystallinity and texture. For the preparation of the TEM lamella, a standard lift-out procedure during focused-ion beam (FIB) milling was utilized (Scios 2 DualBeam system, ThermoFisher Scientific).

For crystallographic investigations, Bragg-Brentano X-ray diffraction was utilized, using a PANalytical XPert Pro MPD system equipped with a Cu-Kα radiation source (wavelength $\lambda = 1.54$ Å).

2.3. Electrochemical corrosion experiments

Linear potentiodynamic polarization experiments were performed using a three-electrode set-up. With a saturated Ag/AgCl reference electrode (SSC), a Pt-counter electrode (CE) and the coated-steel sample as working electrode (WE), the pitting-corrosion resistance was measured in a 0.1 M NaCl solution. Each sample was mounted into a press-fit corrosion cell, accomodating a sample contact area of 1.58 cm^2. All samples were left to equilibrate for 20 min, after which the open circuit potential (OCP) was measured over an additional duration of 5 min. Linear sweep voltammetry (LSV) measurements were started cathodically at OCP- 300 mV and swept into the anodic region with a sweep-rate of 1 mV/s up to + 1.2 V_{SSC}. With a current-density cut-off value set to 1 mA/cm^2, the electrochemical tests were controlled and monitored by a potentiostat (Autolab PGSTAT302N, Metrohm).

Additional cyclic potentiodynamic polarization experiments were carried out using the same three-electrode and potentiostat set-up. In an identical manner, the samples were left to equilibrate for 20 min in a 0.1 M NaCl solution and the OCP was measured over the course of an additional 5 min. With a sweep-rate of 20 mV/min, the measurements were started at OCP, swept to an upper vertex potential of + 1.2 V_{SSC}, and stopped at a potential of −0.8 V_{SSC} (see Fig. 1). If, however, an anodic current limit of 1 mA/cm^2 was reached, the scan direction was reversed instantaneously at the corresponding potential $E_{rev} \leq +1.2$ V_{SSC}.

By conducting Tafel-extrapolations and evaluating the cyclic potentiodynamic polarization curves, electrochemical parameters such as the breakdown voltage (E_b), the passive current density (i_p), as well as the protection or re-passivation potential (E_{prot}) were determined, see Fig. 1.

2.4. Characterization of electrochemically tested surfaces

Corroded samples were embedded in a conductive polymer-matrix, their cross-sections ground and polished, and analyzed via SEM and EDX. Accordingly, pit-formations, coating-substrate adherence, and fast-track diffusion routes of the electrolyte were examined.

High-resolution analytical techniques such as Time-of-Flight Secondary Ion-Mass-Spectroscopy (TOF-SIMS) and Atom Probe Tomography (APT) were consulted for tracing chloride species across pristine coating sites (no macroparticles, pin-holes, voids, etc.). For the TOF-SIMS measurements a TOF-SIMS 5 instrument (IONTOF GmbH, Münster, Germany) was used. Depth profiles were acquired in a high vacuum ($\sim 4{\cdot}10^{-7}$ Pa) using a 25 keV Bi^+ primary ion beam. A high current bunched mode (HCBU) was used for depth profile measurements, which require a high mass resolution and low limit of detection. [18–21] As non-metal elements were the focus of the research, a 2 keV Cesium gun was used as the sputter source with the polarity set to negative and a cycle time of 60 μs. Low energy electron flooding of 21 V was used to reduce surface charging. In HCBU, the analysis area was set

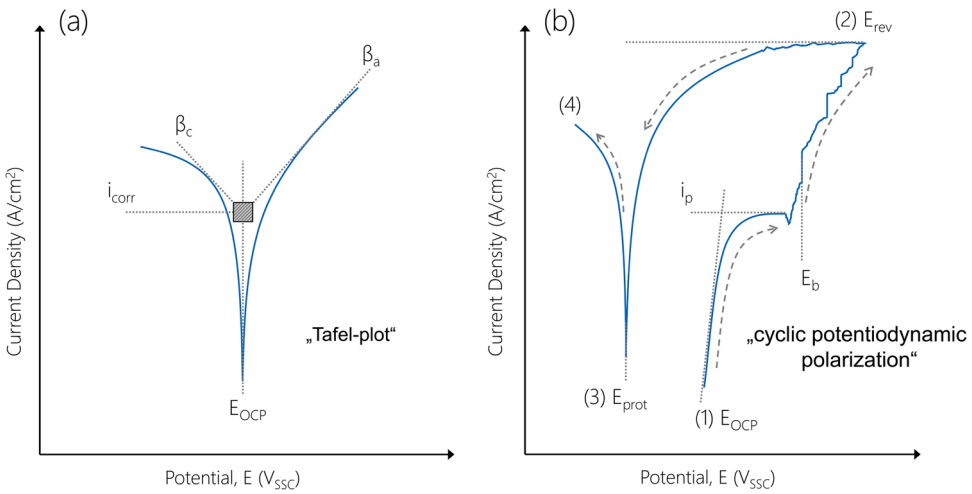

Fig. 1. Schematic of (a) Tafel-Plot and (b) course of a cyclic potentiodynamic polarization measurement. The scan starts with (1) the open circuit potential (OCP), sweeps at 20 mV/min to (2) the reverse potential (E_{rev}) + 1.2 V_{SSC} (or any lower potential if a current density value larger than 1 mA/cm^2 was reached). From E_{rev} the scan returns through (3) the re-passivation/protection potential (E_{prot}) and (4) stops at −0.8 V_{SSC}.

to 100 × 100 μm^2 with 1 shot/pixel, whereas the sputter crater was set to 300 × 300 μm^2 to ensure homogeneous material removal at the measurement site. The measurements were stopped after around 8000s

Lastly, APT was chosen as a quantitative method for measuring the diffused Cl-content within surface-near coating regions. At pristine coating sites of electrochemically stressed samples, tip lift-outs of 2 μm length were prepared by a focused ion beam (Scios 2 DualBeam system, ThermoFisher Scientific). Prior to the milling process, a thin protective tungsten layer was deposited in order to preserve the surface vicinity of the coating. The final sharpening of the tips was performed with 30 kV acceleration voltage and 50 pA, after which a clean-up sequence ensued with 5 kV and 28 pA for generating a Ga damage-free tip. The APT analysis was carried out on a Cameca LEAP 4000X HR in pulsed laser mode, equipped with a 355 nm UV laser and a reflection lens. The experiments were done with a laser pulse energy of 50–90 pJ with a pulse rate of 200 kHz at a target evaporation rate of 1 %, whose mass-spectra were then analyzed using a MATLAB tool-box for quantifying the diffused Cl-contents. [22].

3. Results and discussion

3.1. Microstructure and compositional analysis

The as-deposited SEM cross-sections, as well as respective top-view micrographs are illustrated in Fig. 2 and highlight the intrinsic differences in coating microstructure and texture. Coating thicknesses of 2.5, 5.1, and 7.5 μm were obtained for the arc evaporated depositions, compared to 2.8, 4.9 and 7.1 μm for the sputtered variants (see Fig. 2a-f, respectively). While all coatings feature a typical columnar structure, the sputtered coatings produced a more pronounced and textured morphology. This is related to the inherently lower energetics and ion-flux, as well as lower ion-mobility of arriving species present during sputtering (decreased self-surface diffusion and densification of the coating morphology) [23]. Top-view SEM-micrographs (Fig. 2a*-f*), further highlight the differences in the coating morphology and surface-texturing between arc evaporated and sputtered coatings. Whereas no surface texturing is visible for any of the arc evaporated samples, distinct pyramidal features dominate the surface of the sputtered coatings, particularly with increasing coating thickness (see Fig. 2f*).

Fig. 3 presents the diffractograms and peak-patterns for all as-deposited coatings. All coatings feature a face-centered-cubic (fcc) crystal-structure with mixed [111]/[200] growth orientations. Here as well, the texture of the sputtered coatings stands out, as the diffractograms clearly display a shift from a highly [200] orientated crystal structure (see Fig. 3d) to a preferred [111] crystal orientation (see Fig. 3f), with increasing coating thickness.

All in all, the as-deposited states can be summarized as follows: The arc evaporated coatings share a columnar and dense morphology with a fcc-crystal structure composed of mixed [111] and [200] crystal orientations. Similarly, all sputtered coatings feature a fcc-crystal structure with a pronounced columnar morphology. However, with higher coating thicknesses, the crystal growth orientation changes from a mixed [111]/[200] to a preferred [111] orientation, which results in the formation of a highly faceted surface. Lastly, by utilizing EDX analysis, the metal content ratios for the sputtered- and arc evaporated coatings were determined to be $Al_{0.67}Cr_{0.33}N$ and $Al_{0.68}Cr_{0.32}N$, respectively.

3.2. Electrochemical corrosion properties

The Tafel-plots of the bare 90MnCrV8 alloy and the AlCrN coated samples are shown in Fig. 4a. The corrosion current (i_{corr}) and open circuit potential (E_{OCP}) were determined from the intersection of the extrapolated anodic and cathodic Tafel-branches (Fig. 1a) [27]. All extrapolations were performed manually with no additional software package for data analysis. The corrosion potential of the uncoated steel substrate leveled at about −569 mV_{ssc}, whereas the open circuit potentials of the AlCrN coated samples all settled within the range of −378 mV_{ssc} to −326 mV_{ssc} ($OCP_{(mean)}$= −352 mV_{ssc}), regardless of the deposition route used. The positive shift from −569 mV_{ssc} to −352 mV_{ssc} indicates reduced anodic activity of the AlCrN-coated samples over the bare alloy. Minimal improvement in i_{corr} was measured for all AlCrN coated samples over the bare substrate, again with similar values across all coating variants (see Table 1).

Fig. 4b and c illustrate the cyclic potentiodynamic polarization curves of all arc evaporated coatings and sputtered coatings, respectively. Starting from the corrosion potential (E_{OCP}) and sweeping into the anodic region, all samples show a similar corrosion behavior. From about +100 mV_{ssc} upwards, the AlCrN-coated samples enter their passive region, where the current densities (i_{pass}) of the sputtered coatings measure slightly lower than those of the arc evaporated variants. Also within each coating group (sputtered and arc evaporated), the obtained passive current values decrease with increasing coating thickness (see Table 1). Despite being rather small reductions in the measured currents, it may be suggestive of a sealing-effect of initial defect sites and open porosities. In other words, initial fast-track diffusion routes may be

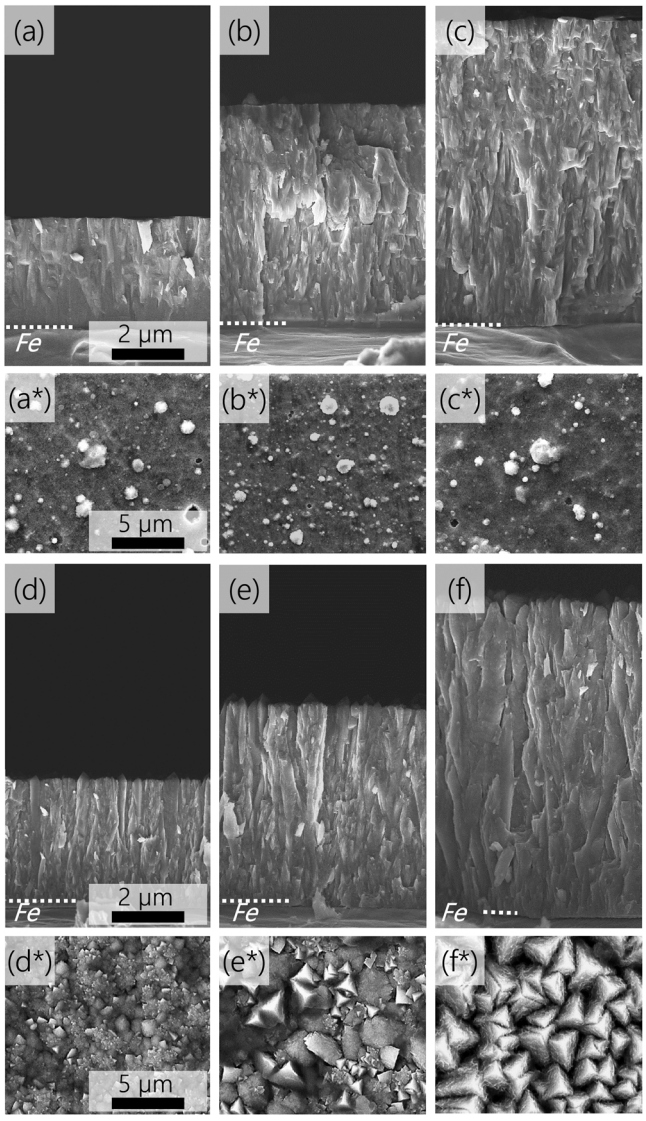

Fig. 2. As-deposited SEM cross-sections of arc evaporated coatings (a-c) with thicknesses of 2.5, 5.1, and 7.5 µm, and sputtered coatings (d-f) with thicknesses of 2.8, 4.9 and 7.1 µm, respectively. Related top-view morphologies are shown in (a*-f*).

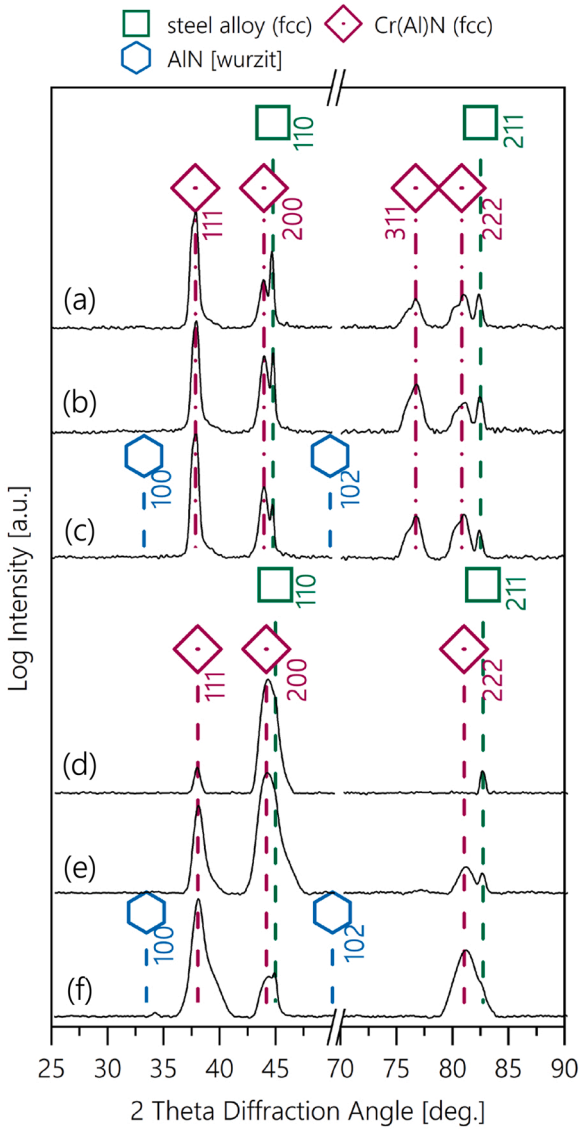

Fig. 3. XRD spectra of the as-deposited arc evaporated fcc-AlCrN coatings (a-c) with thicknesses of 2.5, 5.1 and 7.5 µm, respectively, as well as sputtered fcc-AlCrN coatings (d-f) with thicknesses of 2.8, 4.9, and 7.1 µm, respectively. Reference patterns were taken from Ref. [24–26].

overgrown by longer deposition times and result in an improved passive behavior of the coating. When increasing the applied potential further, all measurements indicate a drop in the current density values at ~300 mV_{ssc}, followed by a spike in the measured current shortly after, which we interpreted as the breakdown potential (E_b) for each coating. This is indicative for the equilibria reaction $Fe^{2+}+2OH^- \rightarrow Fe(OH)_2$, prematurely passivating the pit-mouth openings. Subsequent internal acidification then leads to a rapid elevation in the alloy dissolution and drastically increases the corrosion current values. Interestingly, despite the coating thickness within the arc evaporated and sputtered groups, all arc evaporated AlCrN samples reach the current cut-off value (1 mA/cm^2) at similar potentials (E_{rev}= ~360 mV_{ssc}), whereas E_{rev} for all sputtered variants is found more anodic (E_{rev}= ~420–450 mV_{ssc}). A summary of the electrochemical properties is presented in Table 1. Together with the results from the Tafel-plots, these findings further strengthen the argument, that coating thickness plays a subordinate role in the corrosion mechanism of AlCrN-coated low alloy steel samples. For this reason, from here onwards, further investigations will focus solely on the ~5 µm thick arc evaporated- and sputtered coatings.

3.3. Morphological investigations of preferential pitting sites

SEM cross-sections of the electrochemically stressed AlCrN samples are shown in Figs. 5–7, highlighting the preferred diffusion pathways and pit-initiation sites for both, arc evaporated and sputtered coating variants. Cross-sections of the arc evaporated AlCrN samples (see Figs. 5 and 6) evidently single out intrinsically deposited macroparticles as the dominating weak-spot for pit-formations. Fig. 5a shows the polished cross-section of an as deposited arc evaporated AlCrN coating. Visible through the mass-contrast is the bright chrome-rich inner core of the droplet, which has been verified by EDX analysis. Also highlighted are porous domains below the core that have evolved through shadowing effects throughout the growth of the macroparticle. While exposed to NaCl-rich aqueous media during electrochemical testing, these metallic cores are prone to accelerated oxidation. Whereas some droplets only suffer premature oxidation (Fig. 5b), others oxidize much more severely, depending on how coherently the droplets sit within the coating matrix. Fig. 5c and the respective EDX line-scan illustrate such a matured state. Specifically, the EDX line-scan emphasizes the oxygen enriched

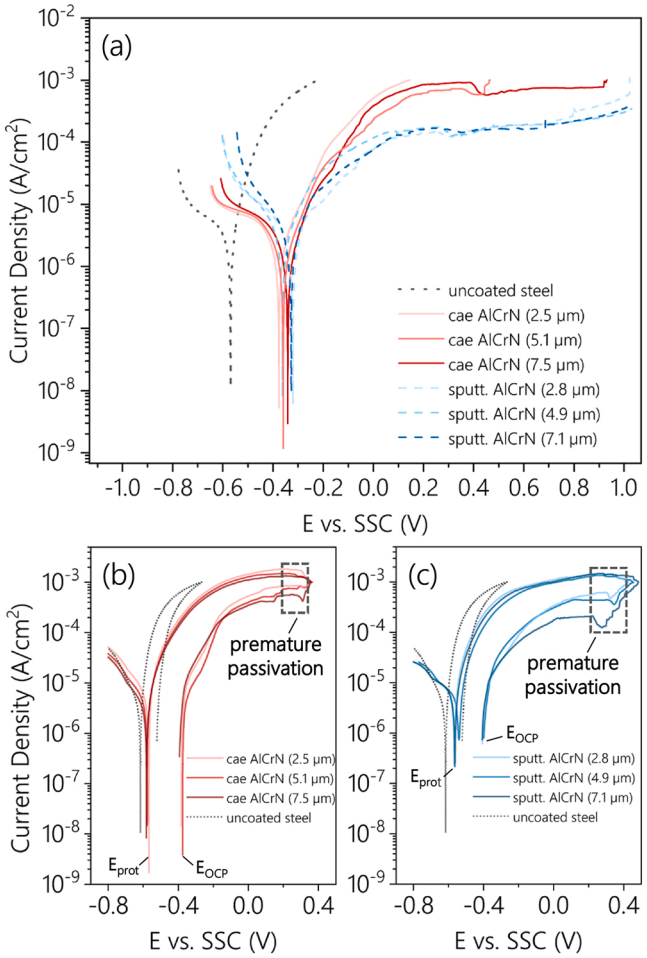

Fig. 4. Electrochemical measurements in 0.1 M NaCl solution: (a) Tafel-Plots of cae-AlCrN coatings (solid red lines), sputtered-AlCrN coatings (dashed blue lines), and uncoated low alloy steel substrate (dotted grey line), (b-c) cyclic potentiodynamic polarization curves of cae-AlCrN coatings and sputtered-AlCrN coatings, respectively.

chromium core, as well as surrounding areas, where the corrosive media has permeated the droplet-coating boundaries.

Particularly, droplets located near the coating-substrate interface and permeate the entire coating structure (see Fig. 6a-c), offer fast-track diffusion routes along the particle-coating interface. Once a pit has initiated (Fig. 6b), the exchange of both, corrosion product out of the pit, as well as transport of the aqueous media into the pit, occurs simultaneously along these pathways. In Fig. 6d and the respective EDX maps this ion-exchange is further exemplified. While the pristine coating matrix remains chemically and structurally unchanged (alloy and metallic droplets are the only chemically active species) an accelerated metal dissolution of the substrate is observed (pit growth).

Fig. 7, on the other hand, illustrates the most abundantly observed pit-initiation route for the sputtered AlCrN coating. Owed to the inherently fewer number of defect-sites, other diffusion routes must be present. The cross-sections in Fig. 7a-c reveal vertical channels that form throughout the corrosion experiments. Analogous to the diffusion paths along macroparticle boundaries in arc evaporated coatings, these channels allow for inward and outward diffusion of corrosion products and chloride/hydroxide-ions. The formation of channels can be related to the more pronounced columnar morphology of the sputtered coatings, as well as the intrinsically lower packing/density of the overall microstructure. Similar to the arc evaporated sample, Fig. 7d and the respective EDX maps suggest that the surrounding sputtered AlCrN coating matrix is chemically stable. Homogeneous distribution of aluminum and chromium, with no indication of coating deterioration through oxidation confirms this impression. Furthermore, the EDX maps highlight the exchange of iron and oxygen between the pit and surface by channels that trend along the column boundaries.

3.4. Surface near examination of chloride inward diffusion by APT

In order to reveal more about the actual passivity of the intact coating morphology to chloride species (no fast-track diffusion pathways, e.g. droplets, macroparticles and/or underdense columnar morphology), APT lift-outs were taken from pristine coating sites of cyclic potentiodynamic polarized samples (see Fig. 4). Fig. 8a shows the positions chosen for the lift outs, whereas Fig. 8b-c illustrate two of the tip preparation steps (milling and sharpening, respectively). The mass spectra of the corroded arc evaporated coatings (see Fig. 8d) and sputtered coating (see Fig. 8e) originate from the surface near regions of the electrochemically stressed coatings. These spectra quantitatively highlight the amount of diffused chloride for the duration of the corrosion experiment. Labeled are the individual chlorine-containing fragments that substantiate the presence of diffused chloride species through the pristine coating morphologies. The interpretation and quantification of the dataset (chlorine containing signals) render a chloride concentration of 600 ppm for the arc evaporated coating, whereas a 28 times higher chloride concentration of 16,800 ppm was determined for the sputtered AlCrN film (comparing the same volume). This clearly demonstrates that pristine coating morphologies, particularly the topmost regions, are indeed permeable to chloride. As expected, a significantly lower chloride concentration was measured for the arc evaporated coating, suggesting that the arc evaporated coating has a more coherent and compact coating morphology than its sputtered equivalent. This also emphasizes the dominant role of embedded macroparticles in the pitting initiation mechanism of arc evaporated coatings. In contrast,

Table 1
Electrochemical properties from the cyclic potentiodynamic polarization experiments in 0.1 M NaCl solution. E_{OCP}, corrosion potential; E_{prot}, protection potential; E_b, breakdown potential; i_p, passive current density; i_{corr}, corrosion current density.

Coating	Thickness (µm)	E_{OCP} (mV_{ssc})	E_{prot} (mV_{ssc})	E_b (mV_{ssc})	i_p (A/cm^2)	i_{corr} (A/cm^2)
bare alloy	–	-569	-616	–	–	2.65×10^{-6}
cae-AlCrN	2.5	-381	-567	324	$7.52 \times 10^{-4} \pm 1.10 \times 10^{-5}$	9.76×10^{-7}
	5.1	-374	-576	318	$5.13 \times 10^{-4} \pm 5.28 \times 10^{-5}$	8.87×10^{-7}
	7.5	-392	-580	334	$4.01 \times 10^{-4} \pm 1.13 \times 10^{-5}$	9.11×10^{-7}
sputt.-AlCrN	2.8	-406	-567	329	$5.56 \times 10^{-4} \pm 4.92 \times 10^{-6}$	1.09×10^{-6}
	4.9	-398	-539	357	$4.36 \times 10^{-4} \pm 3.91 \times 10^{-6}$	1.54×10^{-6}
	7.1	-405	-562	371	$1.92 \times 10^{-4} \pm 5.47 \times 10^{-6}$	1.51×10^{-6}

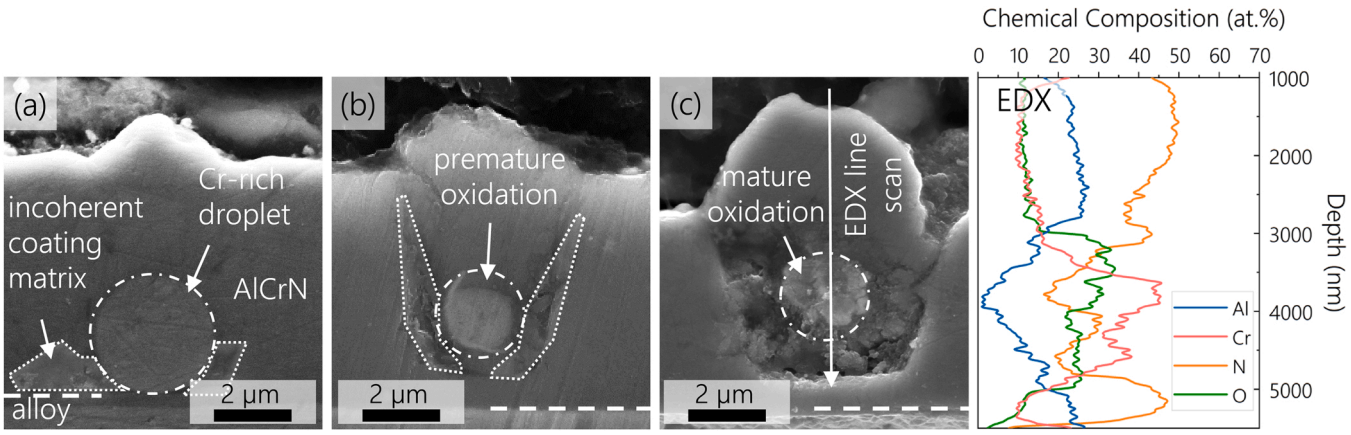

Fig. 5. SEM cross-section images of (a) as deposited arc evaporated- AlCrN coating, (b) prematurely corroded droplet within the arc evaporated AlCrN coating matrix, and (c) matured corrosion of the metallic droplet core with the respective EDX analysis as indicated by the arrow.

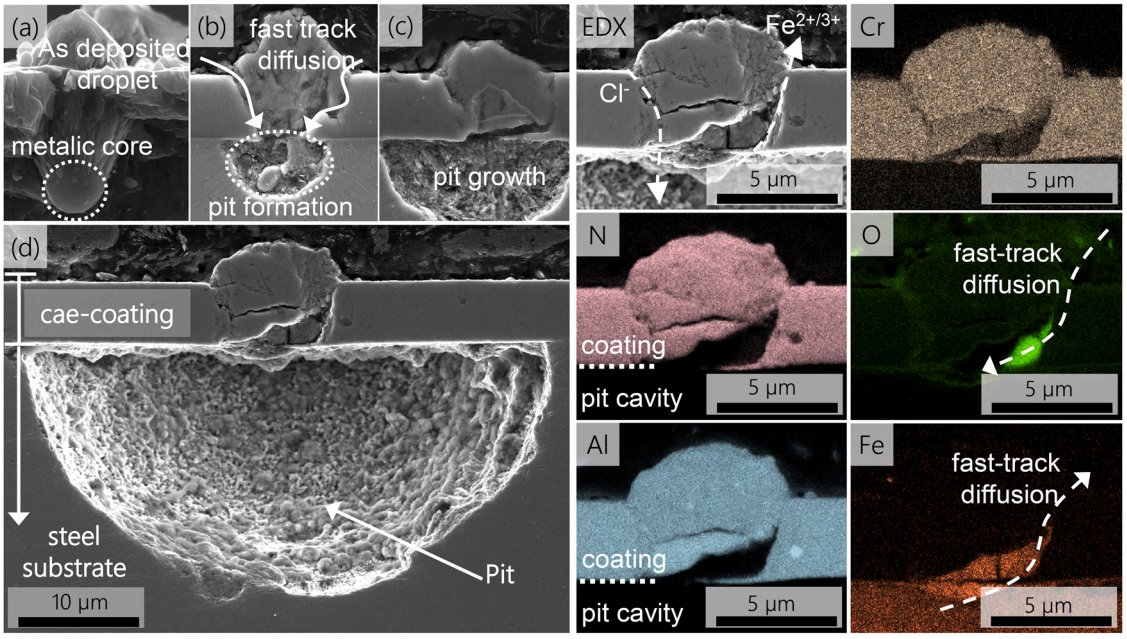

Fig. 6. SEM investigations of preferred diffusion routes in cae-AlCrN coatings: (a) as-deposited droplet routed within the coating matrix; (b-c) pit initiation and propagation stages; (d) fully developed pit cavern with respective EDX color maps that highlight diffusion exchange pathways between cavity and coating surface.

significantly higher chloride concentrations were measured for the sputtered AlCrN coating. With its more directional columnar growth and inferior packing density, the sputtered coating matrix proves extremely pervious to chloride and provides no adequate diffusion barrier. In order to extend the scope from coating surface near regions towards the coating-substrate interface, it was of great interest to examine the chloride diffusion across the overall coating thickness.

3.5. Depth profiling of chloride diffusion by TOF-SIMS

In order to investigate the chloride diffusion qualitatively throughout the entire span of the pristine coating matrix, TEM analysis, as well as TOF-SIMS depth-profile measurements were carried out for both, arc evaporated (Fig. 9a-e) and sputtered coatings (Fig. 9f-j). Selected area electron diffractograms (SAED) and TEM bright field images of the measured coatings provide localized information about the coating's crystallinity and help to interpret the obtained TOF-SIMS data. The collected depth-profiles of the anionic Cl and Al species are presented in Fig. 9e and j, respectively. Based on this analysis, the progression of chloride (diffusion front) was assessed. While the dotted lines represent the measurements of the as-deposited samples (considering a native Cl-contamination), the solid profiles represent the measurements of the electrochemically stressed samples. The shaded regions enclosed by both, solid and dotted lines, highlight the loading behavior and diffusion front in both, cae and sputtered samples.

By looking at the depth-profiles of the arc evaporated AlCrN coatings, a more or less typical diffusion curve is observed (Fig. 9e). With a chloride-enriched surface region, reaching about 500 nm into the coating, a gradual decline in chloride concentration follows for about 3 µm, after which the concentration gradient bleeds out at the coating substrate interface. When examining the respective bright-field TEM image in Fig. 9d, a homogeneous morphology with discontinuous column boundaries is featured. SAEDs of the surface near (Fig. 9a), centered (Fig. 9b) and interface near regions (Fig. 9c) exhibit random crystal orientations of the coating matrix with defined diffraction dots.

On the other hand, Fig. 9j shows the chloride diffusion behavior of the electrochemically stressed sputtered AlCrN coating, featuring a uniform chloride loading profile. Only towards the coating-substrate

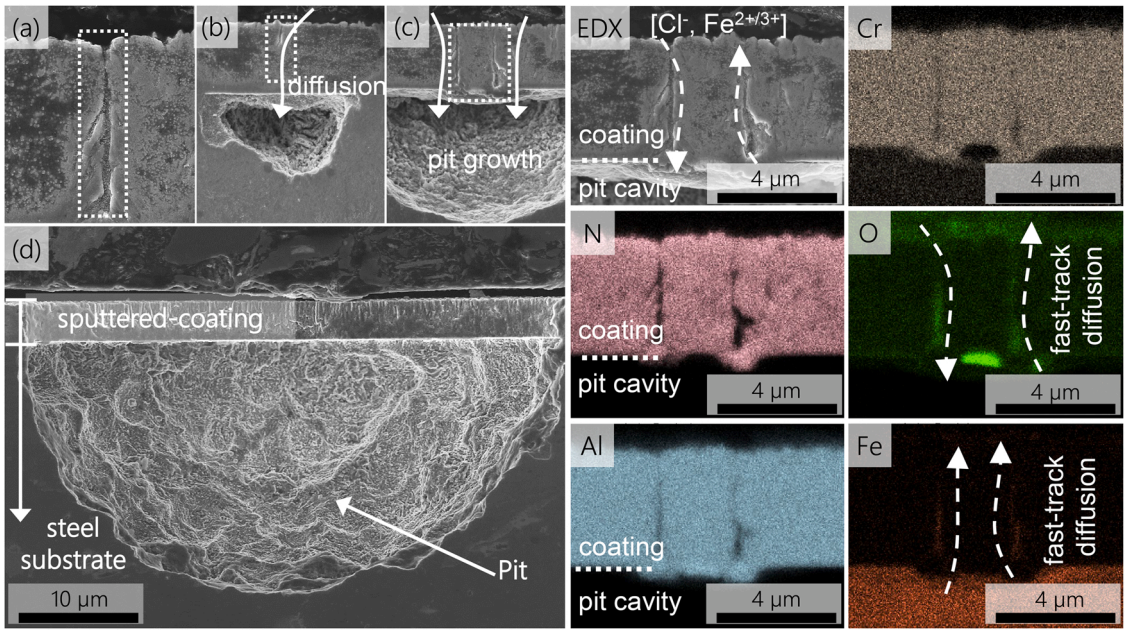

Fig. 7. SEM investigations of preferred diffusion routes in sputtered-AlCrN coatings: (a) incoherent column boundary; (b-c) pit initiation and propagation stages; (d) fully developed pit cavern with respective EDX color maps that highlight diffusion exchange channels between cavity and coating surface.

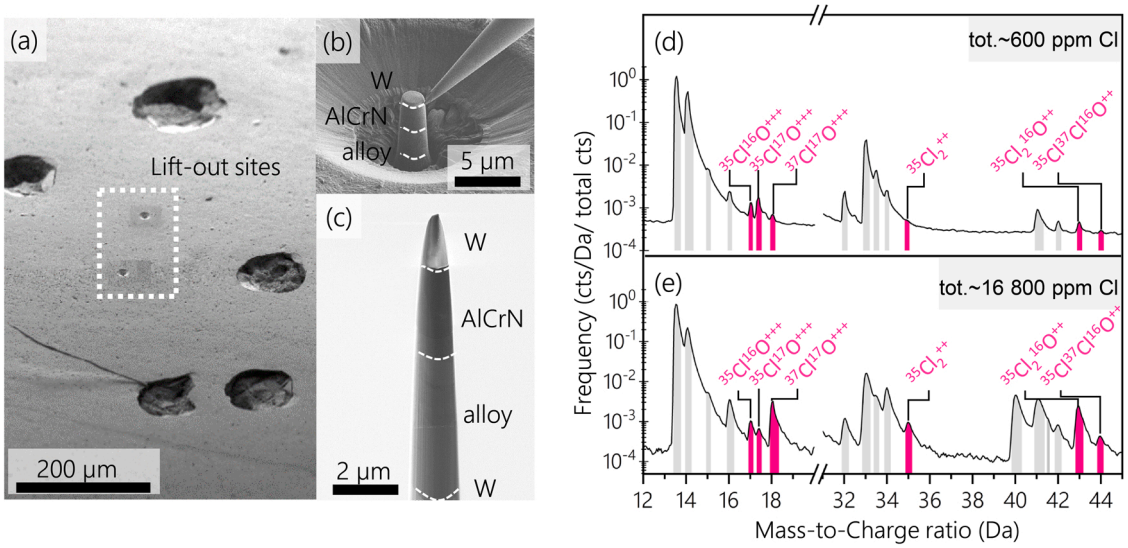

Fig. 8. Illustration of (a) the APT tip-site selection (b) lift-out operation and (c) sharpening sequence of a stressed arc evaporated AlCrN coating. (d) Features the APT mass-spectra of the arc evaporated and (e) of the sputtered coatings. Two cut-outs (12–20 Da & 30–45 Da) highlight the chloride-containing fragments, as labeled, whose integration was used to quantify the respective Cl-contents.

interface, a decrease in the chloride concentration occurs. Evident from the TEM bright-field images and SAED patterns, the difference in the diffusion profile must be, at least partially, due to the variation in the microstructure. Whereas the SAEDs that were collected near the surface and center of the coating show diffraction patterns with distinct diffraction dots, the SAED from near the coating-substrate interface features smeared dots, indicative of a more nanocrystalline microstructure. It may be this property that translates to an improved diffusion barrier, and is responsible for the prevention of pitting at the coating-substrate interface. This may also explain why the corrosion behavior did not improve with increasing coating thickness.

Overall, it can be asserted that the arc evaporated AlCrN morphology exhibits a relatively uniform grain size distribution throughout the entire coating thickness, providing a sufficient diffusion barrier for the duration of the corrosion experiments (diffusion front ~3.2 µm into the sample). Moreover, the sputtered microstructure features an increasing grain and column size distribution from the interface to the surface near regions that allow for accelerated chloride loading throughout most of the coating thickness until the nanocrystalline morphology at the interface is reached (diffusion front ~4.8 µm into the sample).

3.6. *Preferred growth orientations and coating texture*

Lastly, it was of great interest to further substantiate the aforementioned differences in microstructure, especially grain orientation and grain-size distribution. For this, we resorted to transmission electron back-scatter diffraction and performed an averaged evaluation of the grain-size distribution of the AlCrN-coated samples. In this case, the goal

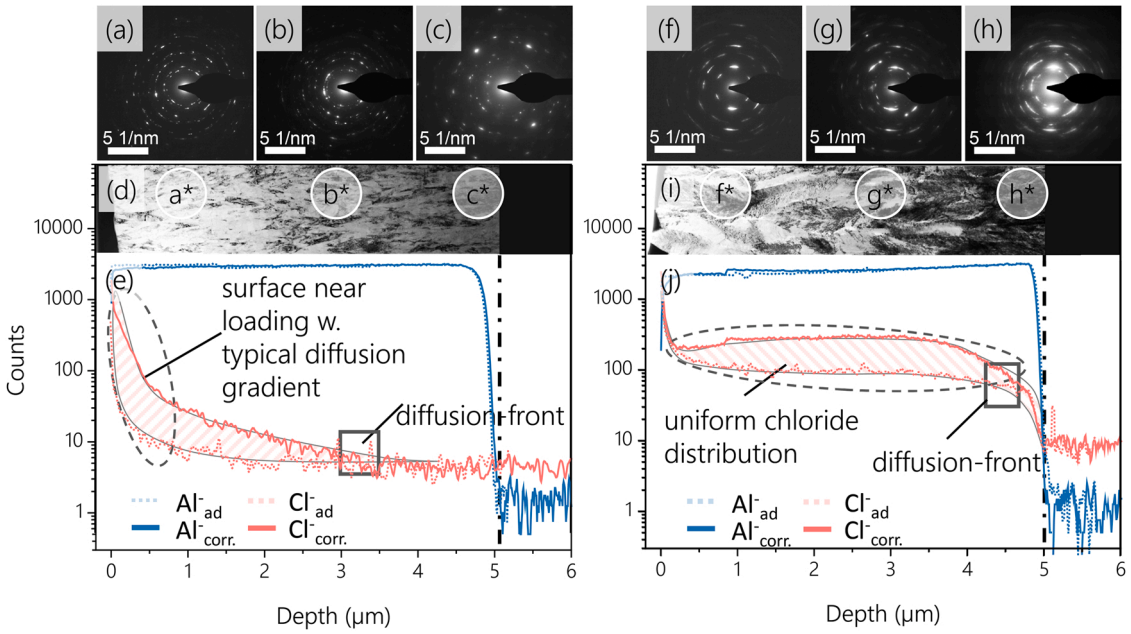

Fig. 9. TEM and TOF-SIMS analysis: (a-c) SAED images indicating differences in crystallinity of surface-near, centered, and interface near arc evaporated coating regions, respectively; (d) bright-field TEM image of the arc evaporated coating morphology; (e) TOF-SIMS depth-profile highlighting the chloride inward diffusion gradient (shaded region) and diffusion front (box) of the arc evaporated AlCrN coating. The illustrations (f-j) corresponds to the sputtered coating variant with identical assignment.

was to link the diffusion profiles obtained from the TOF-SIMS and APT analysis, to the morphological characteristics observed during TEM. Fig. 10 shows the TEM lamellas of the ~5 μm thick arc evaporated and sputtered AlCrN coatings (see Fig. 10a and d), the respective inverse pole figure maps (Fig. 10b and e), as well as inverse pole figures (Fig. 10c and f) calculated from the t-EBSD data. Correlating with the results from the XRD analysis, the inverse pole figures reveal a highly orientated {001} growth direction for the 5 μm sputtered coating, whereas a mostly random growth orientation, with a weak preference in the {211} plane, is featured by the arc evaporated coating variant. At this point, we would like to point out that the difference in the color range interval used for the arc evaporated sample (Fig. 10c) and sputtered-sample (Fig. 10f). Whereas the {211} orientation of the arc evaporated morphology occurs merely three times as often as for a random distribution of christallographic orientations, the {001} orientation in the sputtered matrix appears more than twenty times as often.

From the EBSD data, averaged grain sizes of 72 and 120 nm in horizontal diameter were calculated for the as-deposited arc evaporated and sputtered samples, respectively. These numbers, again substantiate the notion that the highly orientated {001} morphology and the larger grain sizes, in combination with the open column boundaries of the sputtered sample, allow for unimpeded diffusion along its grain boundaries. In this manner, fast bridging of the protective coating and subsequent pit initiation at the coating-substrate interface is granted in a similar way, as would be observed for arc evaporated coatings with their droplet-streaked morphology.

4. Conclusion

With near to identical pitting behavior by electrochemical investigation, in-depth analysis of AlCrN thin films has yielded distinct diffusion mechanisms that pertain exclusively to either arc evaporated or sputtered AlCrN coating morphologies.

For arc evaporated AlCrN coatings, fast-tracked diffusion of the electrolyte was exclusively observed along incoherently incorporated macroparticles, resulting in rapid oxidation of the metallic cores and a consequent dislodging from their surrounding coating structure. It has been found that the formation of cavities functions as the most frequently observed pit-initiation site. Delving deeper into other possible diffusion routes, pristine coating sites (droplet free) were investigated by APT and TOF-SIMS. Both analyses revealed surface near inward diffusion of chloride (600 ppm Cl), however no chloride was detected close to the coating-substrate interface. Featuring a depth profile with a rapidly decreasing chloride concentration gradient, the pristine coating morphology demonstrates excellent diffusion resistance against chloride species. By consulting t-EBSD for a detailed understanding of the coating structure, we appoint the fine-grained morphology (~70 nm) and randomly orientated growth orientation as one of the decisive properties for improved diffusion resistance.

On the other hand, the most abundantly observed pit-initiation mechanism for the sputtered AlCrN samples resulted from diffusion routes along open column domains. The partially coarse-grained microstructure and unidirectional column growth facilitated fast-track diffusion to the coating-substrate interface, allowing for an eased breaching of the coating structure. APT and TOF-SIMS analysis of pristine coating sites exhibited uniform chloride loading throughout most of the sputtered morphology (16800 ppm Cl), which is 28 times higher than for the arc evaporated coating. Unlike for the arc evaporated coating, t-EBSD of the sputtered sample revealed a coarse-grained morphology (~120 nm) with significant coating texturing in the {100} direction. A sufficient diffusion barrier was only observed at the coating-substrate interface, where a sufficiently fine-grained microstructure, as well as randomized growth orientations prevailed.

To perfectly protect the underlying alloy and to prevent pitting, sufficient diffusion resistance to Cl^- must be warranted by the AlCrN coating morphology. Despite being chemically inert to the oxidative electrolyte, both, sputtered and arc evaporated coatings have shown distinctly different diffusion routes, which allow for the initiation of pits at the coating-substrate interface.

CRediT authorship contribution statement

O. E. H. and H. R. conceived the research. L. S. and O. E. H. conducted the coating depositions, as well as the electrochemical corrosion

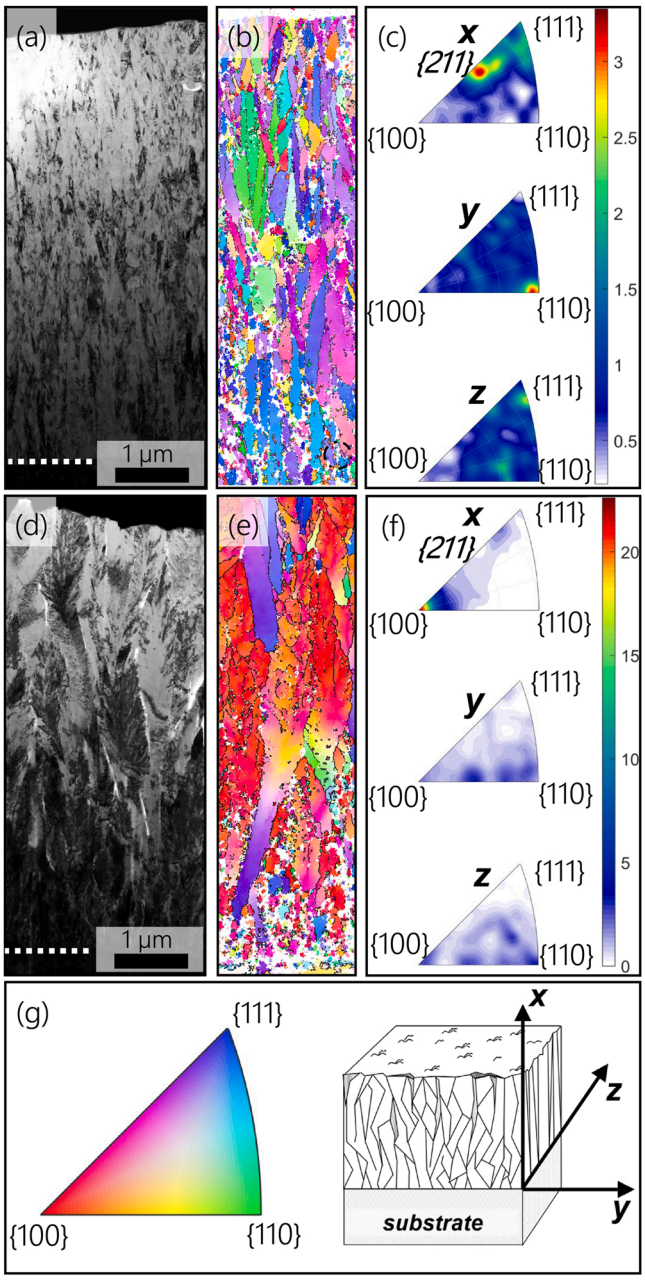

Fig. 10. TEM bright-field images (a, d), EBSD inverse pole figure maps colored with respect to x (b, e) and related inverse pole figures for directions x, y and z (c, f), of the as-deposited arc evaporated and sputtered coatings, respectively. (g) shows the color legend and viewing direction for the IPF maps.

tests. G. B. assisted with the set-up of the electrochemical methods and provided support with their implementation and evaluation. P. K. prepared the TEM and t-EBSD lamella, whereas T. W. conducted the TEM and t-EBSD measurements. R. S. assisted in the evaluation and interpretation of the t-EBSD data. A. B., M. H. and P. F. conducted the preparation and measurements of the atom probe tips, whereas F. B. carried out the ToF-SIMS measurements. O. H. and P. P. supported the research by providing indispensable funding, while L. S. assisted the research with her thematic expertise. H. R. also provided funding acquisition and oversaw the research as supervisor. Finally, all authors have contributed in revising and approving the final version of the manuscript.

Declaration of Competing Interest

The authors declare the following financial interests/personal relationships which may be considered as potential competing interests: Oliver E. Hudak reports financial support was provided by Christian Doppler Research Association.

Data availability

Data will be made available on request.

Acknowledgments

The financial support by the Austrian Federal Ministry for Digital and Economic Affairs, the National Foundation for Research, Technology and Development and the Christian Doppler Research Association is gratefully acknowledged (Christian Doppler Laboratory "Surface Engineering of high-performance Components"). We also thank for the financial support of Plansee SE (Austria), Plansee Composite Materials GmbH (Germany), and Oerlikon Balzers, Oerlikon Surface Solutions AG (Liechtenstein). In addition, we want to thank the X-ray center (XRC) of TU Wien for beam time as well as the electron microscopy center - USTEM TU Wien - for providing the SEM and TEM facilities. The authors acknowledge TU Wien library for financial support through its Open Access Funding Program.

Appendix A. Supporting information

Supplementary data associated with this article can be found in the online version at doi:10.1016/j.corsci.2022.110901.

References

[1] K.V. Akpanyung, R.T. Loto, Pitting corrosion evaluation: a review, J. Phys. Conf. Ser. 1378 (2019), https://doi.org/10.1088/1742-6596/1378/2/022088.
[2] P. Aldhous, R. Akid, R. Leiva-Garcia, S. Zhou, Evaluating the effects of environmental aging on the pitting corrosion of steam turbine blade steels, Mater. Corros. (2022), https://doi.org/10.1002/maco.202213384.
[3] Y. Mollapour, E. Poursaeidi, O. Pedram, Study of pitting corrosion under actual operating conditions of a first stage compressor blade, Eng. Fail. Anal. 131 (2022), 105822, https://doi.org/10.1016/j.engfailanal.2021.105822.
[4] H. DorMohammadi, Q. Pang, P. Murkute, L. Árnadóttir, O.B. Isgor, Investigation of chloride-induced depassivation of iron in alkaline media by reactive force field molecular dynamics, Npj Mater. Degrad. 3 (2019), https://doi.org/10.1038/s41529-019-0081-6.
[5] L. D'Avico, R. Beltrami, N. Lecis, S.P. Trasatti, Corrosion behavior and surface properties of PVD coatings for mold technology applications, Coatings 9 (2019) 1–12, https://doi.org/10.3390/coatings9010007.
[6] A. Perez, A. Billard, C. Rébéré, C. Berziou, S. Touzain, J. Creus, Influence of metallurgical states on the corrosion behaviour of Al-Zn PVD coatings in saline solution, Corros. Sci. 74 (2013) 240–249, https://doi.org/10.1016/j.corsci.2013.04.048.
[7] C. Liu, A. Leyland, Q. Bi, A. Matthews, Corrosion resistance of multi-layered plasma-assisted physical vapour deposition TiN and CrN coatings, Surf. Coat. Technol. 141 (2001) 164–173, https://doi.org/10.1016/S0257-8972(01)01267-1.
[8] P. Panjan, M. Čekada, M. Panjan, D. Kek-Merl, F. Zupanič, L. Čurković, S. Paskvale, Surface density of growth defects in different PVD hard coatings prepared by sputtering, Vacuum 86 (2012) 794–798, https://doi.org/10.1016/j.vacuum.2011.07.013.
[9] P. Panjan, A. Drnovšek, P. Gselman, M. Čekada, M. Panjan, T. Bončina, D.K. Merl, Influence of growth defects on the corrosion resistance of sputter-deposited TiAlN hard coatings, Coatings 9 (2019) 1–16, https://doi.org/10.3390/coatings9080511.
[10] S.B. Abusuilik, K. Inoue, Effects of intermediate surface treatments on corrosion resistance of cathodic arc PVD hard coatings, Surf. Coat. Technol. 237 (2013) 421–428, https://doi.org/10.1016/j.surfcoat.2013.09.026.
[11] H.W. Wang, M.M. Stack, S.B. Lyon, P. Hovsepian, W.D. Münz, The corrosion behaviour of macroparticle defects in arc bond-sputtered CrN/NbN superlattice coatings, Surf. Coat. Technol. 126 (2000) 279–287, https://doi.org/10.1016/S0257-8972(00)00554-5.
[12] M.L. Cedeño-Vente, J. Manríquez, G.C. Mondragón-Rodríguez, N. Camacho, A. E. Gómez-Ovalle, J.M. Gonzalez-Carmona, J.M. Alvarado-Orozco, D.G. Espinosa-Arbelaez, Application of a transmission line model to evaluate the influence of structural defects on the corrosion behavior of arc-PVD CrN coatings, Ceram. Int. (2021), https://doi.org/10.1016/j.ceramint.2021.04.087.

[13] M. Fenker, M. Balzer, H. Kappl, Corrosion protection with hard coatings on steel: Past approaches and current research efforts, Surf. Coat. Technol. 257 (2014) 182–205, https://doi.org/10.1016/j.surfcoat.2014.08.069.
[14] C.M. Koller, S.A. Glatz, S. Kolozsvári, H. Bolvardi, P.H. Mayrhofer, Thermal stability and oxidation resistance of architecturally designed Ti–Al–N- and Ti–Al–Ta–N-based multilayers, Surf. Coat. Technol. 385 (2020), 125444, https://doi.org/10.1016/j.surfcoat.2020.125444.
[15] E. Aschauer, T. Wojcik, P. Polcik, O. Hunold, M. Arndt, V. Dalbauer, P. H. Mayrhofer, P. Felfer, H. Riedl, Ultra-high oxidation resistance of nano-structured thin films, Mater. Des. 201 (2021), 109499, https://doi.org/10.1016/j.matdes.2021.109499.
[16] P. Mohamadian Samim, A. Fattah-Alhosseini, H. Elmkhah, O. Imantalab, Structure and corrosion behavior of ZrN/CrN nano-multilayer coating deposited on AISI 304 stainless steel by CAE-PVD technique, J. Asian Ceram. Soc. 8 (2020) 460–469, https://doi.org/10.1080/21870764.2020.1750102.
[17] D.D. Kumar, N. Kumar, S. Kalaiselvam, S. Dash, R. Jayavel, Wear resistant super-hard multilayer transition metal-nitride coatings, Surf. Interfaces 7 (2017) 74–82, https://doi.org/10.1016/j.surfin.2017.03.001.
[18] A. Benninghoven, Surface analysis by secondary ion mass spectrometry (SIMS), Surf. Sci. 299–300 (1994) 246–260, https://doi.org/10.1016/0039-6028(94)90658-0.
[19] A. Benninghoven, Chemical analysis of inorganic and organic surfaces and thin films by static time-of-flight secondary ion mass spectrometry (TOF-SIMS), Angew. Chem. Int. Ed. Engl. 33 (1994) 1023–1043, https://doi.org/10.1002/anie.199410231.
[20] M. Kubicek, G. Holzlechner, A.K. Opitz, S. Larisegger, H. Hutter, J. Fleig, A novel ToF-SIMS operation mode for sub 100nm lateral resolution: application and performance, Appl. Surf. Sci. 289 (2014) 407–416, https://doi.org/10.1016/j.apsusc.2013.10.177.
[21] R.N.S. Sodhi, Time-of-flight secondary ion mass spectrometry (TOF-SIMS):—versatility in chemical and imaging surface analysis, Analyst 129 (2004) 483–487, https://doi.org/10.1039/B402607C.
[22] P. Felfer, Matlab Toolbox for APT analysis, Github, n.d., (n.d.). ⟨https://github.com/peterfelfer/Atom-Probe-Toolbox⟩.
[23] C. Yang, B. Jiang, Z. Liu, J. Hao, L. Feng, Structure and properties of Ti films deposited by dc magnetron sputtering, pulsed dc magnetron sputtering and cathodic arc evaporation, Surf. Coat. Technol. 304 (2016) 51–56, https://doi.org/10.1016/j.surfcoat.2016.06.083.
[24] International Center of Diffraction Data, Powder diffraction file 01–083-5613, 2016.
[25] International Center of Diffraction Data, Powder diffraction file 00–046-1200, 1996.
[26] International Center of Diffraction Data, Powder diffraction file 04–014-0360, (2010).
[27] R.A. Buchanan, E.E. Stansbury, 4 Electrochemical Corrosion, (2012).